Preprints (www.preprints.org) | NOT PEER-REVIEWED | Posted: 5 July 2017 doi:10.20944/preprints201707.0007.v1

Peer-reviewed version available at Appl. Sci. 2017, 7, 862; doi:10.3390/app7080862

Article

Axial fan blade vibration under inlet cross-flow

Till Heinemann [1] and Stefan Becker [1,*]

[1] Institute of Process Machinery and Systems Engineering, University of Erlangen-Nuremberg, Cauerstr. 4, 91058 Erlangen, Germany; sekretariat@ipat.uni-erlangen.de

* Correspondence: sb@ipat.uni-erlangen.de; Tel.: +49-9131-85-29455

Abstract: In thermal power plants equipped with air-cooled condensers, axial cooling fans operate under the influence of ambient flow fields. Under inlet cross-flow conditions, the resultant asymmetric flow field is known to introduce additional harmonic forces to the fan blades. This effect has previously been studied only numerically or using blade mounted strain gauges. For this study, Laser Scanning Vibrometry was used to assess fan blade vibration under inlet cross-flow conditions in an adapted fan test rig inside a wind tunnel test section. Two co-rotating laser beams scanned a low pressure axial fan, resulting in spectral, phase resolved surface vibration patterns of the fan blades. Two distinct operating points were examined, with and without inlet cross-flow influence. While almost identical fan vibration patterns were found for both reference operating points, overall blade vibration increased by 100% at low fan flow rate due to cross-flow, and by 20% at high fan flow rate. While numerically predicted natural frequency modes could be confirmed from experimental data as minor peaks in the vibration amplitude spectrum, they were not excited significantly by cross-flow. Instead, primarily higher rotation rate harmonics were amplified, i.a. a synchronous blade tip flapping was strongly excited at the blade pass frequency.

Keywords: axial fan; laser scanning vibrometry; wind tunnel; inlet cross-flow; blade vibration

---

1. Introduction

In arid regions, ecologic and economic reasons increasingly demand the application of air-cooled condensers (ACC) in thermal power plants [1]. Traditional "A-frame" designs consist of large diameter, low-pressure axial fans mounted horizontally below bundles of heat exchanger tubes where the condensate is cooled by the fans' draft [2]. At the fans' inlets, the influence of cross-flow induced by neighboring fans and natural ambient winds, which typically reach magnitudes of 5 to 13 m/s or more [3,4], is a major issue. It effectively reduces the volumetric effectiveness of the cooling fans [5–10].

Cross-flow introduces asymmetric effects in the inlet flow field of the fans and cause an azimuthal dependence of the flow's angle of attack at the fan blades. This affects the pressure and velocity distribution at the rotor outlet, as well as the blade loads. The strong asymmetry of the flow field was shown early by Thiart and von Backström [11] for a wall mounted fan, indicating the mechanisms behind the reduction of volumetric effectiveness. For the shrouded peripheral fans in an array of cooling fans of an ACC, the inlet cross draft additionally causes a flow detachment at the windward edge of the nozzle or condenser bank edge. This introduces additional asymmetric effects to the inlet flow field, as shown by Meyer [12] using numerical investigations, and from experimental and numerical data by van der Spuy et al. [13,14].

Along with its negative aerodynamic influence on fan cooling performance, inlet cross-flow is also known to increase blade load and vibration. Depending on its lateral position, relative blade motion is advancing or retreating to the ambient cross-flow, which respectively results in greater or

© 2017 by the author(s). Distributed under a Creative Commons CC BY license.

Preprints (www.preprints.org) | NOT PEER-REVIEWED | Posted: 5 July 2017 doi:10.20944/preprints201707.0007.v1

Peer-reviewed version available at Appl. Sci. 2017, 7, 862; doi:10.3390/app7080862

smaller angle of attack of the relative flow at the fan blade. This may result in greater or smaller blade forces and can lead to considerable stall effects [15]. The upwind inlet shroud detachment can affect the load in longitudinal direction of the cross-flow decisively [16].

Hotchkiss et al. [15] found a strong azimuthal dependence of blade load due to $\gamma = 45°$ between inflow angle and fan axis in a pipe-inlet free-outlet computation. For anti-clockwise fan rotation and inlet cross-flow from the left (azimuthal position $\varphi = 180°$) to the right ($\varphi = 0°$), Hotchkiss et al. found variations in torque and thrust of more than 20% compared to the reference case without cross-flow, with maxima locating around the $\varphi = 180 \ldots 220°$ and minima around $\varphi = 0°$.

Similar results were found from simulation performed by Bredell et al. [16], who computed significant bending moment variations of ACC periphery fans under the influence of induced inlet cross-flow. Azimuthal variation of the load distribution was similar to the findings of Hotchkiss et al, i.e. maximum bending momentum was found at the upwind position $\varphi = 180°$. It was shown that nature and magnitude of the amplification caused by induced cross-flow at the periphery fan depend strongly on ACC platform height and fan geometry. Larger hub to tip ratio fans did not show essentially smaller bending moment variations.

From measurements with strain gauges on an operating on-site periphery fan in a power plant ACC, Muiyser et al. [17] computed the azimuthal load distribution. Their experimental findings agree with the computations mentioned above. Blade load was increased dominantly by magnitudes around 20% at the upwind side of the periphery fan, with higher loads at the advancing blade side ($\varphi \approx 0°$ to $180°$) compared to the retreating blade side. Earlier potential flow computations by Muiyser et al. [18] already identified the sensitivity of blade vibration to distorted inlet flow conditions. Depending on blade stiffness, excitation due to cross-flow was found to lead to considerable damping or resonance effects. Largest strain gauge amplitudes were found where rotation rate frequency harmonics were in proximity of natural frequencies [17,18].

Inlet cross-flow can obviously cause great amplifications in fan vibration and respective blade loads. This is relevant to the effective stress in the large-diameter cantilever style fans used in conventional ACCs. It may also be a concern for larger hub to tip ratio fans, especially when operating rotation rate harmonics coincide with a natural frequency of the blade.

Rather than determining the azimuthal load distribution, this study wants to gain more spatially resolved spectral information on the influence of inlet cross-flow on the blade vibration of axial fans. For this, blade motion was captured using Laser Scanning Vibrometry (LSV) in a wind tunnel fan test rig, as described below. Natural frequencies and mode shapes of the industrial fan were computed, and the findings are used to assess the motion patterns of peak amplitude frequencies from the measurements.

2. Materials and Methods

Laser Scanning Vibrometry measurements were performed on an axial fan, using a fan test rig mounted inside a wind tunnel test section. Natural modes and frequencies were computed from a FEM eigenvalue computation of the fan under centripetal load.

2.1. Wind tunnel fan test rig

The influence of an inlet cross-flow on fan blade vibration was measured using LSV inside a customized fan test rig inside a Göttinger type wind tunnel with a 2.80 m long open test section and an exit nozzle of $1.87 \times 1.40\,\mathrm{m}^2$. A commercial $D_{\mathrm{fan}} = 300\,\mathrm{mm}$ diameter low pressure axial fan with five forward skewed blades and a hub to tip ratio of $\nu_{\mathrm{hub}} = 0.342$ was examined operating with its axis perpendicular to a uniform ambient velocity U_0. Figure 1 shows the experimental setup, and fan design is illustrated in Fig. 2.

Preprints (www.preprints.org) | NOT PEER-REVIEWED | Posted: 5 July 2017 doi:10.20944/preprints201707.0007.v1

Peer-reviewed version available at Appl. Sci. 2017, 7, 862; doi:10.3390/app7080862

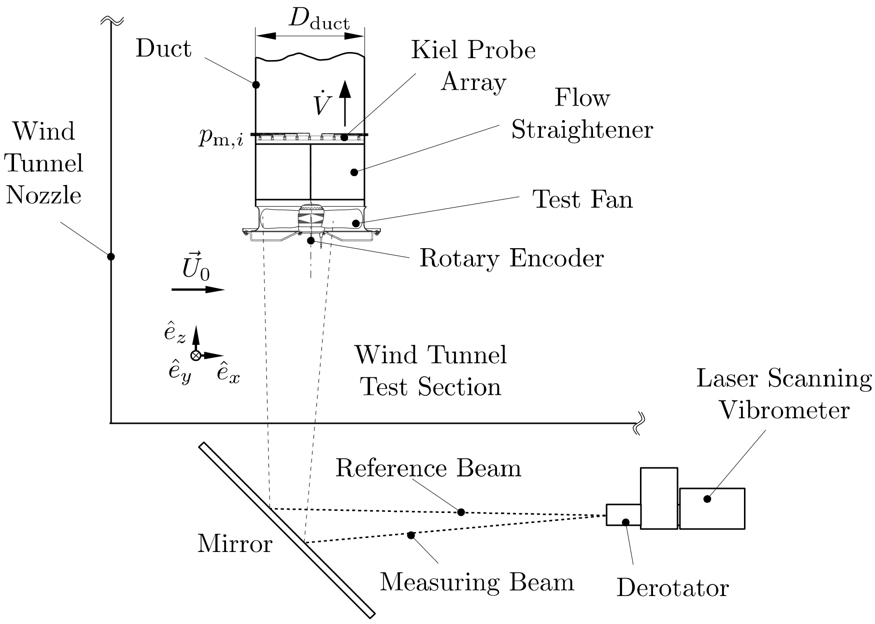

Figure 1. Experimental setup in wind tunnel test section.

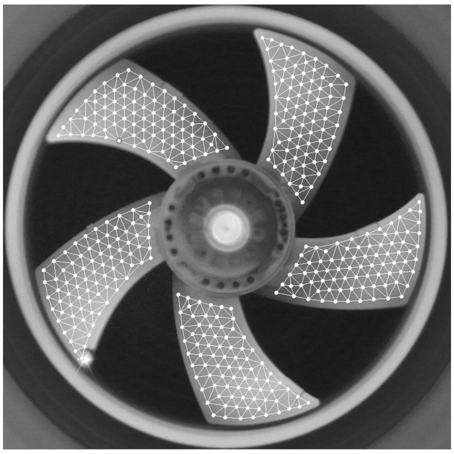

(a) Scan point distribution on rotor at inlet seen from front, anti-clockwise rotation.

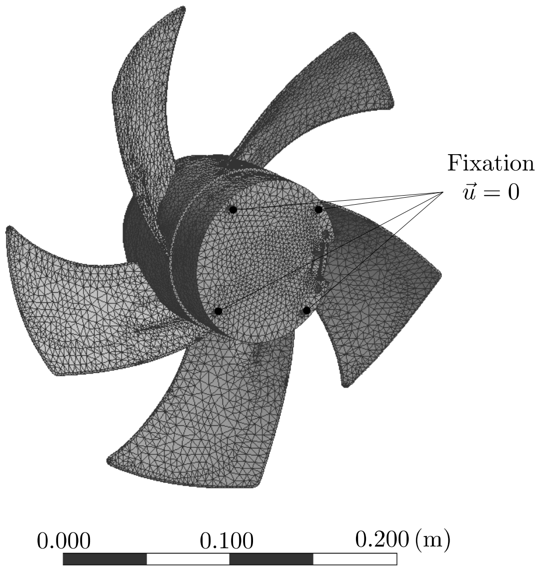

(b) FEM tessellation for natural frequency computation, seen from outlet, clockwise rotation.

Figure 2. Experimental subject axial fan with forward skewed blades.

The test fan was examined operating in its standard shroud without guard grille, held in place by four thin struts with its outlet mounted to a square duct section, $1.5 \cdot D_{\text{fan}}$ above the wind tunnel test section's floor. Behind a short flow straightening device, stagnation pressure $p_{\text{m},i}$ was captured relative to wind tunnel ambient pressure with 81 Kiel type stagnation pressure probes, and surface averaged to the total to total fan pressure $\Delta p_{\text{tt}} = \sum_{i=1}^{81} p_{\text{m},i}/81$. The equally spaced 9×9 grid of pressure probes

Preprints (www.preprints.org) | NOT PEER-REVIEWED | Posted: 5 July 2017 doi:10.20944/preprints201707.0007.v1

Peer-reviewed version available at Appl. Sci. 2017, 7, 862; doi:10.3390/app7080862

inside the $300 \times 300\,\mathrm{mm}^2$ square duct is described in [19]. Fan flow rate $\dot{V}$ was computed from static pressure loss over five standard nozzles inside a settling chamber at the end of the outlet duct in accordance to fan test rig standard ISO 5801 (not displayed in Fig. 1). The experimental setup was previously used to investigate the integral inlet flow field influence on the characteristic fan curve, as shown in [20].

To measure fan rotation rate f_0 and to synchronize the test fan with the co-rotating laser scanning vibrometer's derotator, a rotary encoder was mounted directly to the fan axis at its center. With the wind tunnel either turned off or operating at $U_0 = 10\,\mathrm{m/s}$ wind velocity, the characteristic cross-flow coefficient

$$\mu = \frac{U_0}{\pi D_{\mathrm{fan}} f_0} \tag{1}$$

differed slightly around 0.25, depending on the rotation rate f_0 of the commercial fan.

At one low flow rate OP1 and a higher one OP2 with similar flow rate coefficients

$$\Phi = \frac{4\,\dot{V}}{\pi D_{\mathrm{fan}}^2 \cdot (1 - \nu_{\mathrm{hub}}^2) \cdot \pi D_{\mathrm{fan}} f_0}, \tag{2}$$

a total of four operating points were measured with $\mu = 0$ (OP10 and OP20) and $\mu \approx 0.25$ (OP11 and OP21), as listed in Table 1 along with the respective total fan pressure coefficients

$$\Psi_{\mathrm{tt}} = \frac{2\,\Delta p_{\mathrm{tt}}}{\rho\,(\pi D_{\mathrm{fan}} f_0)^2}. \tag{3}$$

Table 1. Examined operating points

		μ	Φ	Ψ_{tt}	U_0 in m/s	f_0 in Hz	$\dot{V}$ in m^3/s	Δp_{tt} in Pa
OP1	OP10	0.0	0.165	0.148	0.0	43.27	0.412	141.1
	OP11	0.258	0.172	0.112	10.0	41.13	0.408	95.8
OP2	OP20	0.0	0.277	0.092	0.0	44.18	0.706	90.8
	OP21	0.244	0.284	0.015	10.0	43.42	0.717	14.8

2.2. Laser Scanning Vibrometry

Axial blade surface velocity distribution was captured using a Polytec PSV-500 Scanning Vibrometer, coupled with a PSV-A-400 derotator. The laser beam scanned the fan blades' surface at $N_{\mathrm{ScPts}} = 400$ equally distributed probe locations with a typical distance of 10 mm as shown in Fig. 2a, at a sampling rate of 12.5 kHz. On each scanning point, 30 samples of 640 ms (around 27 full fan rotations) were successively captured and transferred to the frequency domain. Hanning windows with 70% overlap were used to average the 30 samples, resulting in frequency domain data sets of bandwidth $B = 5\,\mathrm{kHz}$ resolved to discrete frequencies $k \cdot \Delta f$, with $\Delta f = 1.5625\,\mathrm{Hz}$. With the respective fan rotation rate f_0, discrete Strouhal numbers

$$Sr_k = k \cdot \Delta f / f_0 \tag{4}$$

resulted. Plain kinematic effects were observed at rotation rate f_0, caused by the uncertainty in parallel alignment of laser beam and fan axis. To exclude such rigid body rotation effects from blade vibration analysis, the frequency domain was filtered to a minimum integer k_0 above the second rotation rate harmonic, such that

$$k \in \{k_0, k_0 + 1, \ldots, B/\Delta f\}, \text{ with } k_0 = \left\lceil \frac{2.2\, f_0}{\Delta f} \right\rceil, \text{ and } B/\Delta f = 3200. \tag{5}$$

Preprints (www.preprints.org) | NOT PEER-REVIEWED | Posted: 5 July 2017 doi:10.20944/preprints201707.0007.v1

Peer-reviewed version available at Appl. Sci. 2017, 7, 862; doi:10.3390/app7080862

The scanning laser was accompanied by a reference beam signal $v_{z,\text{ref}}(Sr_k)$, which remained fixed on one probe location for phase reference to the individual measured velocities $v_{z,i}(Sr_k)$ (for $i = 1 \ldots N_{\text{ScPts}}$ scan points). Using the recorded cross spectral density between the two signals $G_{i,\text{ref}}(Sr_k)$, a phase offset of point i at Sr_k

$$\theta_{i,\text{ref}}(Sr_k) = \tan^{-1}\left(\frac{\text{Im}\left\{G_{i,\text{ref}}(Sr_k)\right\}}{\text{Re}\left\{G_{i,\text{ref}}(Sr_k)\right\}}\right) . \tag{6}$$

can be computed. This allows the reconstruction of a relative motion pattern

$$\tilde{v}_{z,i}(Sr_k) = v_{z,i} \cdot \cos\left(\theta_{i,\text{ref}}(Sr_k)\right) . \tag{7}$$

The magnitude of total fan vibration is analyzed with the surface averaged axial velocity as a function of the frequency,

$$v_z(Sr_k) = \frac{1}{N_{\text{ScPts}}} \sum_{i=1}^{N_{\text{ScPts}}} v_{z,i}(Sr_k) . \tag{8}$$

Using this, the integral level of overall fan blade vibration can be expressed by the root mean square value over all Strouhal numbers $k_0 \Delta f / f_0 \leq Sr_k \leq B / f_0$ with k_0 from Eq. (5), i.e.

$$v_{\text{rms}} = \sqrt{\Delta f \cdot \sum_{k=k_0}^{B/\Delta f} \left[v_z(Sr_k)\right]^2} = \sqrt{\Delta f \cdot \sum_{k=k_0}^{B/\Delta f} \left[\frac{1}{N_{\text{ScPts}}} \sum_{i=1}^{N_{\text{ScPts}}} v_{z,i}(Sr_k)\right]^2} . \tag{9}$$

2.3. Numerical setup for natural frequency computation

To interpret the measured vibration shapes at dominant frequencies, the natural frequencies $f_{e,j}$ of the test fan were computed, along with the respective mode shapes. The finite element solver ANSYS Mechanical was used to perform the modal analysis under typical centripetal loads.

Tetrahedral triangulation of the geometric fan model was performed with typical element sizes of $10^{-3} D_{\text{fan}}$, resulting in 206 802 nodes. The resulting mesh is shown in Fig. 2b. A centripetal load was inflicted on the fan at $f_0 = 44.2$ Hz, with rigid support in all degrees of freedom at the four bolt locations marked $\vec{u} = 0$ in Fig. 2b. This resulted in peak von-Mises equivalent stress levels of 269 MPa, located at the leading edge of the blades at around on third of the span between hub and tip. This pre-strain of the blades has a considerable influence on the fan's natural frequencies and mode shapes.

3. Results

3.1. Reference results and computed mode shapes

3.1.1. Natural frequencies

Natural frequency computation with the setup described above typically resulted in groups of five distinct frequencies in great proximity. These refer to the same natural mode for each individual blade, which differ numerically due to model and mesh asymmetries. The arithmetic mean over theses sets of joint frequencies resulted in the first eight natural frequencies $f_{e,j}$ listed in Table 2 along with the respective Strouhal numbers $Sr_{e,j}$, which differ for the different rotation rates f_0 of the four operating points. The distinct five frequencies averaged to $f_{e,j}$ are listed in Table 3 for $j = 1$ to 4.

Preprints (www.preprints.org) | NOT PEER-REVIEWED | Posted: 5 July 2017 doi:10.20944/preprints201707.0007.v1

Peer-reviewed version available at Appl. Sci. 2017, 7, 862; doi:10.3390/app7080862

Table 2. First eight mean natural frequencies computed under centripetal load from rotation at $f_{0,\mathrm{e}} = 44.18\,\mathrm{Hz}$, including natural Strouhal numbers respective to the four operating points.

j	1	2	3	4	5	6	7	8
$f_{\mathrm{e},j}$ in Hz	184.7	432.8	942.8	1123	1657	1948	2034	2190
$Sr_{\mathrm{e},j}$ (FEM)	4.181	9.796	21.34	25.42	37.51	44.09	46.04	49.57
$Sr_{\mathrm{e},j}$ (OP10)	4.269	10.00	21.79	25.95	38.29	45.02	47.01	50.61
$Sr_{\mathrm{e},j}$ (OP11)	4.491	10.52	22.92	27.30	40.29	47.36	49.45	53.25
$Sr_{\mathrm{e},j}$ (OP20)	4.181	9.796	21.34	25.42	37.51	44.09	46.04	49.57
$Sr_{\mathrm{e},j}$ (OP21)	4.254	9.968	21.71	25.86	38.16	44.86	46.85	50.44

Table 3. Blade specific distinct first four natural frequencies.

j	$f_{\mathrm{e},j}$ in Hz	Distinct associated frequency in Hz				
		Blade 1	Blade 2	Blade 3	Blade 4	Blade 5
1	184.7	184.96	184.70	184.72	184.73	184.77
2	432.8	432.71	432.80	432.84	432.88	432.94
3	942.8	942.02	942.10	943.03	943.17	943.57
4	1123	1122.4	1122.5	1122.6	1123.6	1123.6

3.1.2. Spectral decomposition of the surface averaged velocity amplitude

Reference results show the response of fan vibration without the presence of a uniform ambient cross-flow field at the fan inlet ($U_0 = 0\,\mathrm{m/s}$). Dominant amplitude peaks can be determined, and a comparison of the two operating points OP10 and OP20 can be made. Selected frequencies Sr are examined more closely, and the respective reconstructed motion pattern can be compared to associated natural modes determined from FEM simulation.

Figure 3 shows the spectral decomposition of the surface averaged fan blade velocity amplitude v_z from all N_{ScPts} scan points as defined in Eq. (8) for the frequency range $2.2 < Sr \leq 50$. As annotated above, the first two rotation rate harmonics $Sr = 1$ and 2 are cut off due to distortion by kinematic effects. In Fig. 3, dotted vertical lines indicate the harmonics of the blade pass frequency $Sr = 5$. The data sets' natural frequencies $Sr_{\mathrm{e},i}$ are added in dashed vertical lines for $i = 1$ to 4. Due to the different rotation rates f_0 of the operating points' natural frequencies, these dashed lines do not coincide for the data sets.

It becomes clear from Figure 3 that the measured mean surface vibration was dominated by the rotation rate harmonics, i.e. where Sr has integer values, with v_z amplitudes close to zero in between. Even though operating at distinctly different flow rates Φ, the reference spectra of OP10 and OP20 coincide intensely, with almost identical integral vibration measures $v_{\mathrm{rms}} = 362.52\,\mathrm{mm}$ and $363.40\,\mathrm{mm}$, respectively. The dominant peak for both operating points is $Sr = 3$, with similar velocity amplitudes, but also the blade pass frequency harmonics $Sr = 5$, 10 and 15 are prominent. Noteworthy non-integer values Sr locate in the proximity of the first three natural frequencies, especially at $Sr_{\mathrm{e},1}$.

Preprints (www.preprints.org) | NOT PEER-REVIEWED | Posted: 5 July 2017 doi:10.20944/preprints201707.0007.v1

Peer-reviewed version available at Appl. Sci. 2017, 7, 862; doi:10.3390/app7080862

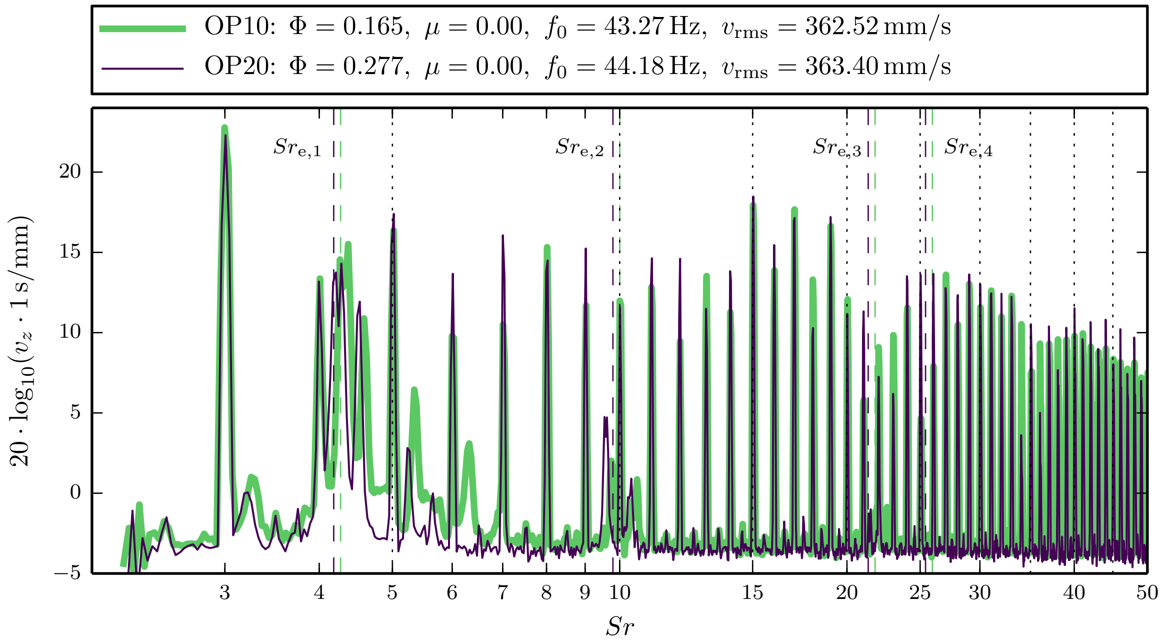

Figure 3. Spectral decomposition of surface averaged blade velocity amplitude over all scan points, without ambient flow.

3.1.3. Mode shapes at natural frequencies

Before the motion patterns at the rotation rate's harmonics are analyzed, the experimental reference results ($\mu = 0$) are compared with the natural frequency computation. The amplitude peaks of the surface average axial velocity $v_z(Sr_{\mathrm{e},1})$ and $v_z(Sr_{\mathrm{e},2})$ from Fig. 3 can dissolved to a relative motion pattern $\tilde{v}_{z,i}(Sr_{\mathrm{e},j})$ using the phase offset to the reference signal, as defined by Eq. (5). In Figs. 4 and 5, the measured reference distribution of $\tilde{v}_{z,i}$ at the discrete frequencies Sr_k of the peaks in very proximity to the first two natural frequencies are displayed on the left.

The exemplary velocity distributions presented in Figs. 4 and 5 belong to the higher flow rate data set OP20. They are also representative for the findings at OP10, which gave very similar results. The images on the right show the mode shapes of the natural frequencies computed by FEM as comparison.

First natural frequency mode

The numerically predicted first natural mode is shown in Fig. 4b. As stated above, five very close frequencies were found for $Sr_{\mathrm{e},1}$, each with another maximum attenuated blade (see Table 3). In Fig. 4b, the left hand blade describes the maximum motion of the first mode. It consists of the flapping of one blade tip leading edge, and a 180 degree counter-motion at a smaller amplitude at the neighboring blades. Two blades in advance (clockwise rotation) from the maximum motion blade, an in-phase motion is detected again.

In the experimental realization of the commercial fan, natural frequencies of the distinct blades are expected to disperse more than in the numerical model, due to manufacturing and installation uncertainties. The combination of the five underlying discrete natural modes of the five blades yielded a range of high amplitude values around $Sr \approx 4.2$ in Fig. 3. At OP20 it resulted in the peak amplitude $v_z(4.173)$, which is dissolved to $\tilde{v}_{z,i}$ in Fig. 4a. The exact same mode shape can be distinguished from the LSV data as predicted from FEM in Fig. 4b. The maximum amplitude blade (bottom position) is flanked by two counter-flapping blades, and one blade in-phase preceding it by two positions. The first natural frequency is visibly a dominant location of vibration, and attention should be paid not to operate the fan at rotation rates such that significant excitation would coincide with $f_{\mathrm{e},1}$.

Preprints (www.preprints.org) | NOT PEER-REVIEWED | Posted: 5 July 2017 doi:10.20944/preprints201707.0007.v1

Peer-reviewed version available at Appl. Sci. 2017, 7, 862; doi:10.3390/app7080862

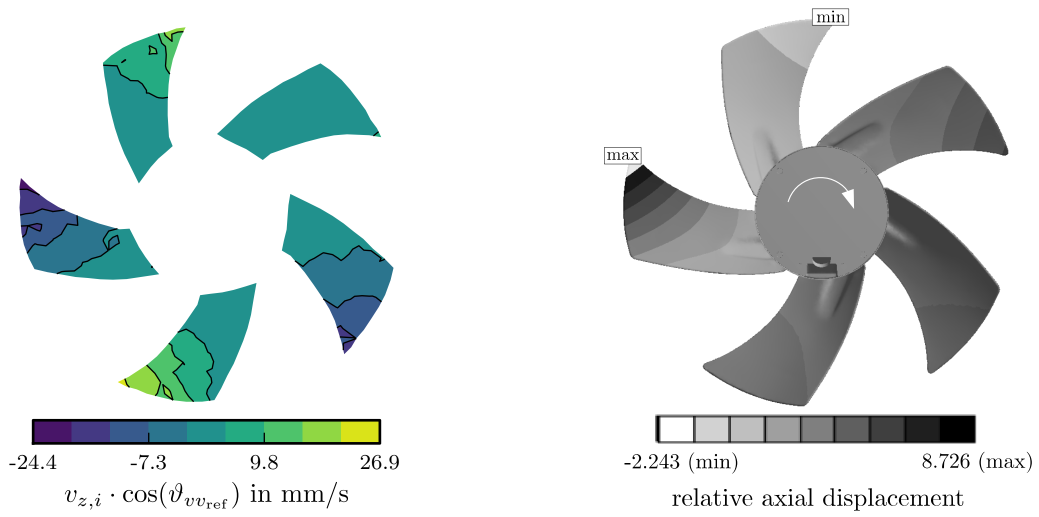

(a) Relative axial velocity distribution $f = 184.375\,\mathrm{Hz}$ ($Sr_k = 4.173$), measured at $\Phi = 0.253$ (OP20).

(b) Computed natural mode under centripetal load at $f_{e,1} = 184.7\,\mathrm{Hz}$ ($Sr_{e,1} = 4.181$)

Figure 4. Measured and computed modal shapes at first natural frequency.

Second natural frequency mode

Compared to $Sr_{e,1}$, the second natural frequency range was measured lower in amplitude $v_z(Sr_{e,2})$ in Fig. 3. The respective predicted mode shape is shown in Fig. 5b. Again, the image refers to one of the five associated distinct frequencies in great proximity, and the blade with maximum attenuation locates on the upper right. The mode bends around a spanwise axis in the blade centerline, with the leading edge swinging in counter-phase to the trailing edge and maximum values at the blade tips. The remaining four non-dominant blades describe a counter-motion to the one on the upper right, with most discernible motion patterns at the two blades opposing it (bottom and left in Fig. 5b).

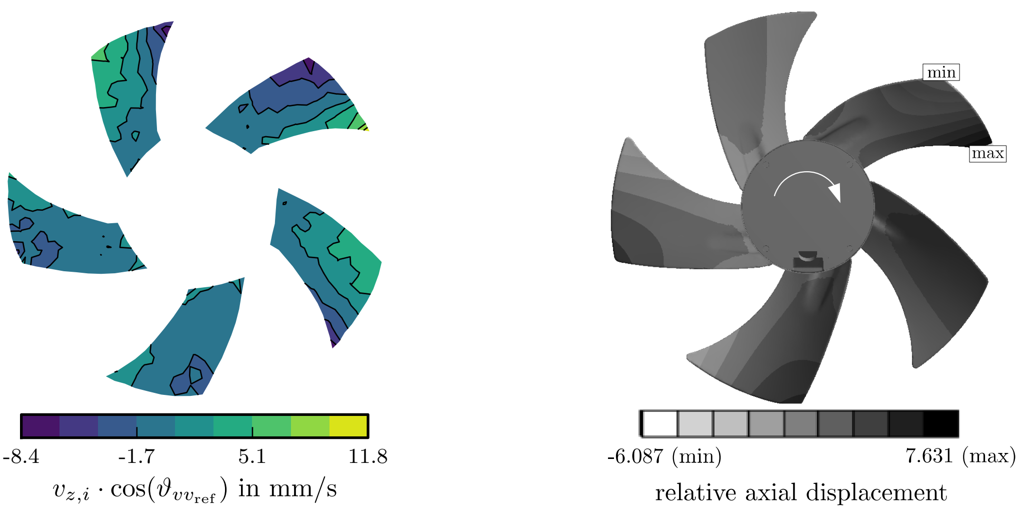

(a) Relative axial velocity distribution $f = 425.0\,\mathrm{Hz}$ ($Sr_k = 9.620$), measured at $\Phi = 0.253$ (OP20).

(b) Computed natural mode under centripetal load at $f_{e,2} = 432.8\,\mathrm{Hz}$ ($Sr_{e,2} = 9.796$).

Figure 5. Measured and computed modal shapes at second natural frequency.

Preprints (www.preprints.org) | NOT PEER-REVIEWED | Posted: 5 July 2017 doi:10.20944/preprints201707.0007.v1

Peer-reviewed version available at Appl. Sci. 2017, 7, 862; doi:10.3390/app7080862

In reference to the associated amplitude peak $v_z(Sr_{e,2})$ in Fig. 3, the relative axial motion $\tilde{v}_{z,i}(9.620)$ is displayed in Fig. 5a for OP20. Again, the mode shape resembles the computation very strongly, with the dominant blade on the upper right. The single difference between measured vibration response and computation may be discerned in the motion of the remaining four blades. The two opposing blades do not show a counter-motion to the upper right one. Instead, such motion is more strongly found in the blades flanking the dominant one. This discrepancy between measurement and computation may be attributed to the differences due to manufacturing and installation, and the interaction of presumably more distinct individual natural frequencies for each blade.

3.2. Inlet cross-flow influence on fan blade vibration

3.2.1. Spectral decomposition of surface averaged vibration

The measured response in surface averaged blade vibration $v_z(Sr)$ to inlet cross-flow is shown in its spectral decomposition in Fig. 6 for OP1 and Fig. 7 for OP2. The integral root mean square measures show a distinct increase in overall blade vibration at OP1 from $\mu = 0.26$. With 718.46 mm/s at OP11, v_{rms} was almost double the value of reference configuration OP10 ($v_{\mathrm{rms}} = 362.52$ mm/s). At OP2, $\mu = 0.25$ cross-flow increased v_{rms} by about 20% from 363.40 mm/s (OP20) to 436.87 mm/s (OP21).

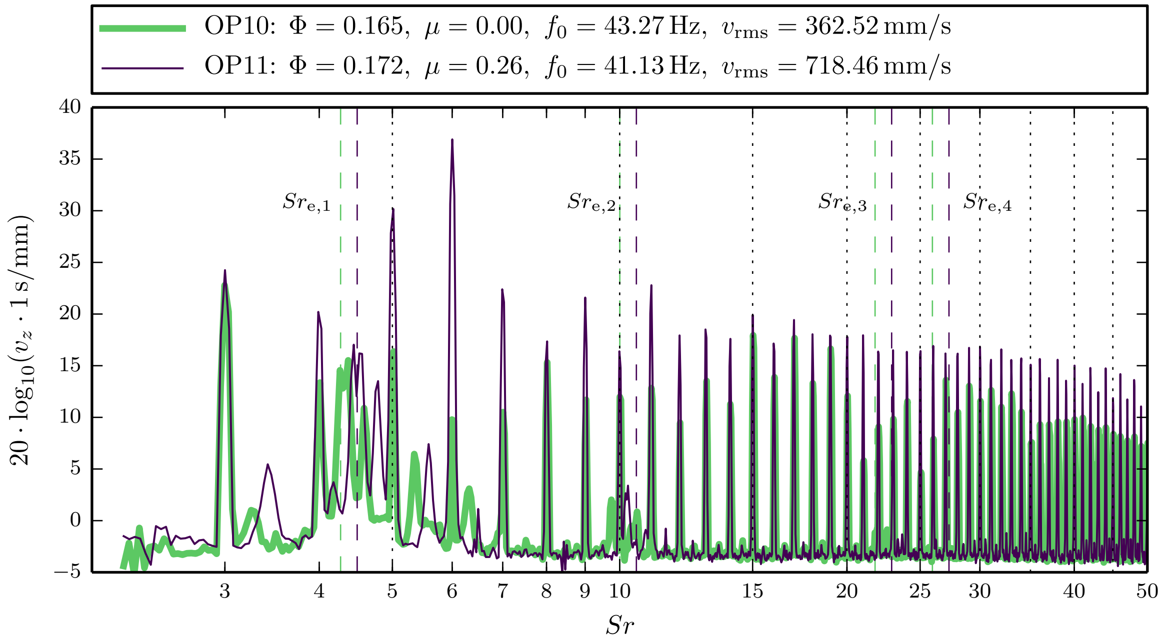

Figure 6. Spectral decomposition of cross-flow influence on measured mean surface velocity amplitude at OP1.

The greater overall increase in v_{rms} also reflects in the influence of cross-flow in the spectral decomposition of $v_z(Sr)$ in Figs. 6 and 7. Amplitude gains are found at OP1 in Fig. 6 at almost each integer value $Sr \geq 4$, but $Sr = 5$ and $Sr = 6$ are the rotation rate harmonics that are exited dominantly. Due to the influence of inlet cross-flow, the blade pass frequency was also measured to become the dominant amplitude peak v_z at the higher flow rate operating point OP2, as visible in Fig. 7. Amplification at $Sr = 6$ was found for OP21 too, but to a far lesser magnitude than for OP1 in Fig. 6. The previously dominant frequency $Sr = 3$ was not affected in amplitude by cross-flow at either operating point.

Preprints (www.preprints.org) | NOT PEER-REVIEWED | Posted: 5 July 2017 doi:10.20944/preprints201707.0007.v1

Peer-reviewed version available at *Appl. Sci.* **2017**, *7*, 862; doi:10.3390/app7080862

Blade vibration around the natural frequency domains cannot be discerned from the data presented in Figs. 6 and 7, the cross-flow influence appears not to excite the fan's natural modes significantly.

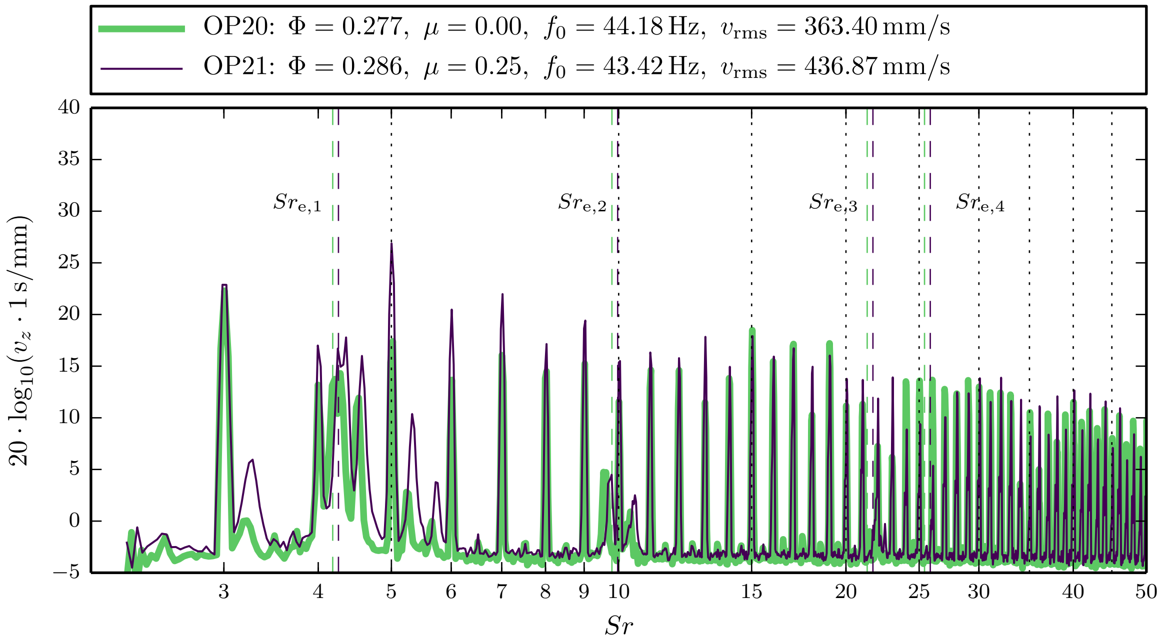

Figure 7. Spectral decomposition of cross-flow influence on measured mean surface velocity amplitude at OP2.

3.2.2. Motion patterns at dominant peaks

The measured relative axial velocity distribution $\tilde{v}_{z,i}$ associated with the dominantly increased frequencies $Sr = 5$ and 6 are compared to the reference results in Figs. 8 to 11.

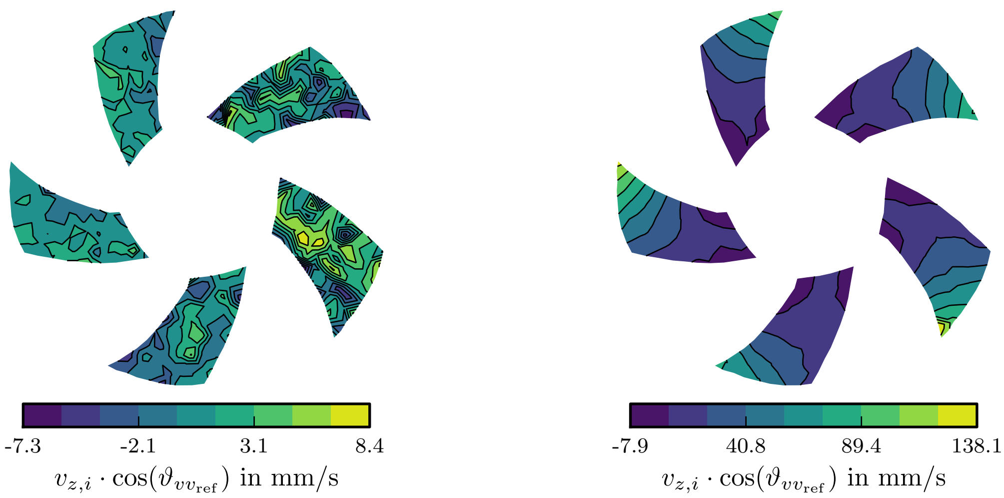

(a) OP10: $\Phi = 0.163$, $\mu = 0$

(b) OP11: $\Phi = 0.166$, $\mu = 0.26$

Figure 8. Cross-flow influence on blade vibration at blade passing frequency $Sr = 5$, OP1.

Preprints (www.preprints.org) | NOT PEER-REVIEWED | Posted: 5 July 2017 doi:10.20944/preprints201707.0007.v1

Peer-reviewed version available at Appl. Sci. 2017, 7, 862; doi:10.3390/app7080862

In all reference results (on the left in Figs. 8 to 11), the distribution of $\tilde{v}_{z,i}$ forms no clear pattern, and the amplitude range is comparably low. In contrast to this, the right hand graphics in Figs. 8 to 11 show very characteristic motion patterns of the fan blades under the influence of inlet cross-flow.

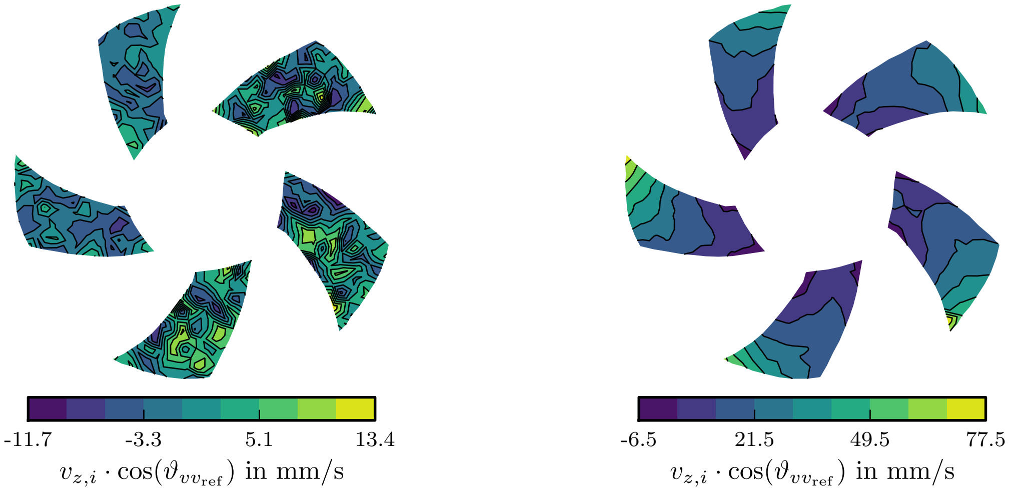

(a) OP20: $\Phi = 0.253$, $\mu = 0$.

(b) OP21: $\Phi = 0.255$, $\mu = 0.24$.

Figure 9. Cross-flow influence on blade vibration at blade passing frequency $Sr = 5$, OP2.

At the blade passing frequency $Sr = 5$, both operating points OP11 (Fig. 8b) and OP21 (Fig. 9b) showed a synchronized blade tip flapping motion caused by the influence of cross-flow. At the blade tips, large peak velocity amplitudes $\tilde{v}_{z,i}(5)$ can be found. The vibration increase at blade pass frequency is not surprising. Since $Sr = 5$ is the frequency at which the fan blades pass the inlet cross-flow, it is also the excitation frequency of the resultant external harmonic forces, causing an in-phase motion of all blades.

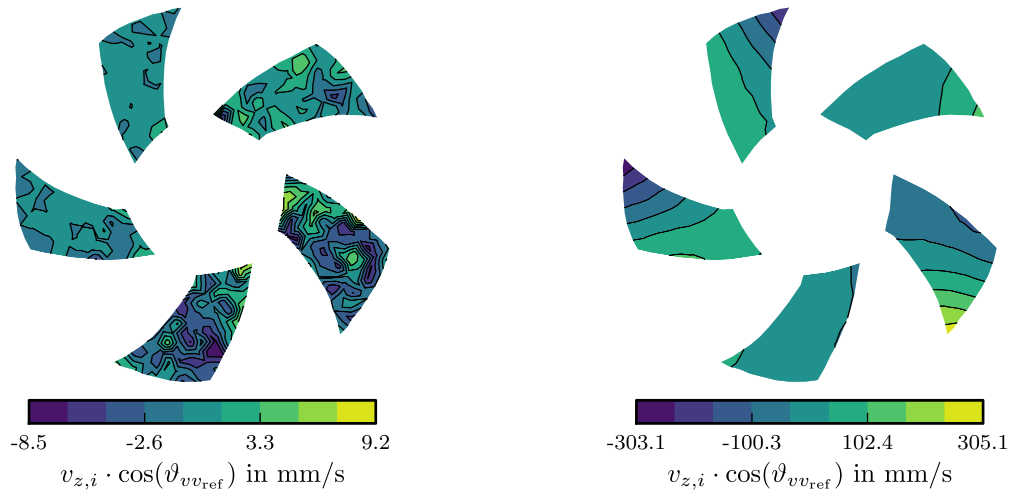

(a) $\Phi = 0.163$, $\mu = 0$

(b) $\Phi = 0.166$, $\mu = 0.26$

Figure 10. Cross-flow influence on blade vibration at $Sr = 6$, OP1.

Preprints (www.preprints.org) | NOT PEER-REVIEWED | Posted: 5 July 2017 doi:10.20944/preprints201707.0007.v1

Peer-reviewed version available at Appl. Sci. 2017, 7, 862; doi:10.3390/app7080862

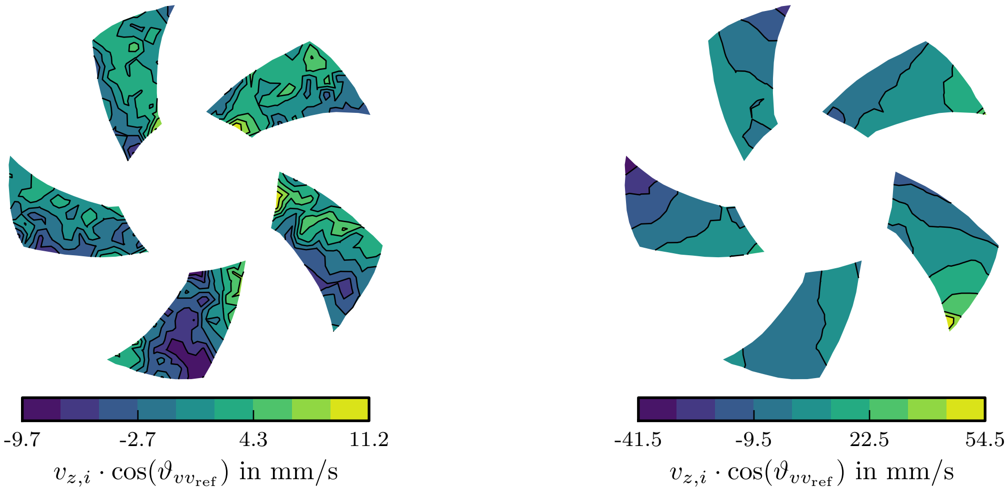

(a) $\Phi = 0.253$, $\mu = 0$

(b) $\Phi = 0.255$, $\mu = 0.24$

Figure 11. Cross-flow influence on blade vibration at $Sr = 6$, OP2.

A blade tip flapping motion was also detected from experimental LSV data at the sixth rotation rate harmonic $Sr = 6$. The pattern can be seen especially clearly for the strong excitation at OP12 in Fig. 10b, but also in Fig. 11b for OP22. But while the single-blade motion with its peak at the leading edge tip resembles the first natural mode shown in Fig. 4b, the dominant blade's neighbors do not move in counter-phase to it. Instead, they have an offset of $\theta_{i,\mathrm{ref}}$ around 90°, which levels the otherwise similar amplitude $v_{z,i}$ at the bottom and upper right blades in Figs. 10b and 11b.

From the fact that blade root amplitudes $\tilde{v}_{z,i}(6)$ are distinctly below zero where the blade tip is maximum (bottom right blade in Fig. 10b), and above zero were blade tip velocity is minimum (left and top blade), an non-ideally stiff fixation of the fan motor to the casing is indicated. Thus, an overlying additional resonance mode of the entire fan within its casing could be the cause of the observed excitation at $Sr = 6$.

4. Discussion

Using a co-rotating LSV setup, it was possible to measure blade vibration of an axial fan with high spectral and spatial resolution. Additionally, the experiment was set up inside a wind tunnel test section to investigate the effect a uniform inlet cross-flow on fan blade vibration, which is known to introduce a significant axial asymmetry of the flow field in the rotor section [12–14].

Up to this point, similar investigations have only been made numerically [15,16,18] or using strain gauges on larger diameter fans [17,21]. Using LSV in this setup, it was possible to gain more insight on the spatial resolution of the fan blade vibration under cross-flow influence, and to compare the resulting motion distributions to numerical mode analysis.

Two distinct fan operating points were examined, with very similar spectral distributions of surface averaged blade vibration amplitude in the reference configuration, i.e. without ambient flow field. The first and, to a smaller extend, second natural frequency showed peaks in the vibration amplitude spectrum which fitted the predicted natural mode very well in shape, but stronger blade vibration was measured at the rotation rate harmonics. Under the influence of inlet cross-flow, the blade pass frequency and the sixth rotation rate harmonic were excited strongly, while no significant amplification of the natural frequencies was measured. These findings agree with previously observed cross-flow excitation effects [17,18]. Integral fan blade vibration almost doubled at low fan flow rate, and increased by 20% at the higher fan flow rate.

Peer-reviewed version available at Appl. Sci. 2017, 7, 862; doi:10.3390/app7080862

While a synchronous flapping of all five blades' tips was observed to be instigated at the blade pass frequency, the nature and cause of the sixth rotation rate harmonic's excitation remains uncertain. It may be attributed to an additional resonance effect of the combined elastic system including the fan and its fixation to the duct section, which was not represented in the modal computation setup.

The experimental results help to identify the affected frequencies and respective mode shapes under cross-flow excitation. Measuring capacity restrictions allowed for few configurations only, so obviously is would be interesting to modify e.g. fan blade shape, hub and shroud shape, and cross-flow coefficients. A generic fan is suggested with more perfect axial alignment to better eliminate perspective distortion. Attention has to be paid to realize a maximum rigid fan axis fixation in the test rig. For future investigation it is also advised to record not only relative phase relation of the measured scanning points, but also identify the azimuthal position in relation to the cross-flow. Such results could yield a better comparison to the findings of e.g. Muiyser et al. [17,18,21].

Acknowledgments: The research leading to these results has received funding from the European Union's Seventh Framework Programme (FP7/2007-2013) under grant agreement number 256797, within the "MACCSol" project. The authors thank Polytec Inc. for their support.

Author Contributions: Till Heinemann and Stefan Becker conceived and designed the experiments, Till Heinemann performed the experiments, analyzed the data, and wrote the paper.

Abbreviations

The following abbreviations are used in this manuscript:

ACC	Air-cooled condenser
LSV	Laser scanning vibrometry
FEM	Finite element method
OPxy	Operating point x with ($y = 1$) or without ($y = 0$) cross-flow

References

1. Maulbetsch, J.S. Cost/Performance Comparisons of Water Conserving Power Plant Cooling Systems. ASME 2011 Int Mech Eng Cong Exp. ASME, 2011, pp. 385–390.
2. Duvenhage, K.; Kröger, D. The influence of wind on the performance of forced draught air-cooled heat exchangers. *J Wind Eng & Industr Aerodynamics* **1996**, *62*, 259–277.
3. Owen, M.; Kröger, D.G. Contributors to increased fan inlet temperature at an air-cooled steam condenser. *Appl Therm Eng* **2013**, *50*, 1149 – 1156.
4. Butler, C.; Grimes, R. The effect of wind on the optimal design and performance of a modular air-cooled condenser for a concentrated solar power plant. *Energy* **2014**, *68*, 886 – 895.
5. Salta, C.; Kröger, D. Effect of inlet flow distortions on fan performance in forced draught air-cooled heat exchangers. *Heat Recovery Systems and CHP* **1995**, *15*, 555–561.
6. Owen, M.T.F.; Kröger, D.G. An Investigation of Air-Cooled Steam Condenser Performance Under Windy Conditions Using Computational Fluid Dynamics. *J Eng Gas Turb & Power* **2011**, *133*, 064502.
7. Borghei, L.; Khoshkho, R.H. Computational fluid dynamics simulation on a thermal power plant with air-cooled condenser. *Proc Inst Mech Eng, A: J Power & Energy* **2012**, *226*, 837–847.
8. Zhang, X.; Chen, H. Performance Forecast of Air-Cooled Steam Condenser under Windy Conditions. *J Energy Eng* **2015**, *142*, 04015010.
9. Xiao, L.; Ge, Z.; Du, X.; Yang, L.; Xu, Z. Operation of air-cooling CHP generating unit under the effect of natural wind. *Appl Therm Eng* **2016**, *107*, 827 – 836.
10. Fourie, N.; van der Spuy, S.; von Backström, T. Simulating the effect of wind on the performance of axial flow fans in air-cooled steam condenser systems. *J Therm Sci Eng Appl* **2015**, *7*, 021011.
11. Thiart, G.; von Backström, T. Numerical simulation of the flow field near an axial flow fan operating under distorted inflow conditions. *J Wind Eng & Industr Aerodynamics* **1993**, *45*, 189–214.
12. Meyer, C. Numerical investigation of the effect of inlet flow distortions on forced draught air-cooled heat exchanger performance. *Appl Therm Eng* **2005**, *25*, 1634–1649.

Preprints (www.preprints.org) | NOT PEER-REVIEWED | Posted: 5 July 2017 doi:10.20944/preprints201707.0007.v1

Peer-reviewed version available at *Appl. Sci.* **2017**, *7*, 862; doi:10.3390/app7080862

13. van der Spuy, S.; von Backström, T.; Kröger, D. Using computational fluid dynamics to simulate multiple axial flow fans in air-cooled steam condensers. ASME 2011 Power Conference collocated with JSME ICOPE 2011, 2011, pp. 375–383.
14. van der Spuy, S.J.; von Backström, T.W. An evaluation of simplified CFD models applied to perimeter fans in air-cooled steam condensers. *Proc Inst of Mech Eng Part A: J Power & Energy* **2015**, pp. 948–967.
15. Hotchkiss, P.; Meyer, C.; von Backström, T. Numerical investigation into the effect of cross-flow on the performance of axial flow fans in forced draught air-cooled heat exchangers. *Appl Therm Eng* **2006**, *26*, 200–208.
16. Bredell, J.; Kröger, D.; Thiart, G. Numerical investigation into aerodynamic blade loading in large axial flow fans operating under distorted inflow conditions. *R & D Journal of SAIMechE* **2006**, *22*, 11–17.
17. Muiyser, J.; Els, D.N.; van der Spuy, S.J.; Zapke, A. The determination of fan blade aerodynamic loading from a measured response. Proc ASME Turbo Expo 2015; ASME., Ed.; , 2015; Vol. 1.
18. Muiyser, J.; Els, D.N.; van der Spuy, S.J.; Zapke, A. Investigation of Large-Scale Cooling System Fan Blade Vibration. ASME Turbo Expo 2014: Turbine Technical Conference and Exposition, 2014.
19. Heinemann, T.; Bakeberg, C.; Lienhart, H.; Becker, S. Total Pressure Measurements Behind an Axial Ventilator Using a Kiel Probe Array. In *New Res in Num & Exp Fluid Mech IX*; Dillmann, A.; Heller, G.; Krämer, E.; Kreplin, H.P.; Nitsche, W.; Rist, U., Eds.; Springer, 2014; Vol. 124, *Notes on Num Fluid Mech & Multidisc Design*, pp. 573–581.
20. Heinemann, T.; Becker, S. Experimental Investigation of Ambient Wind Influence on the Performance of Axial Fans. Proc ASME Turbo Expo 2014. ASME, 2014. GT2014-26468.
21. Muiyser, J.; Van der Spuy, S.; Els, D.; Zapke, A. Measurement of air flow and blade loading at a large-scale cooling system fan. *R & D Journal, of the South African Institution of Mechanical Engineering* **2014**, *30*, 30–38.